Science AAAS

El Niño-Like Pattern in Ice Age Tropical Pacific Sea Surface Temperature

Athanasios Koutavas, *et al.*

Science **297**, 226 (2002);
DOI: 10.1126/science.1072376

Atmospheric CO_2 and N_2O

The most compelling argument for an El Niño–stadial link may be the atmospheric CO_2, CH_4, and N_2O records from ice cores (*31–33*). The atmospheric concentration of each of these gas species increased during interstadials, although the variations were small. The primary source of preindustrial atmospheric N_2O, CH_4, and CO_2 is from the tropics. Upwelling in the tropical Pacific is the largest atmospheric source of CO_2 and a major source of N_2O (*32*). Tropical soils constitute the other primary source of N_2O, and these are major sources of CH_4. El Niño events disrupt the flux of CO_2 and N_2O to the atmosphere as upwelling in the eastern equatorial Pacific is reduced or shut down. Similarly, shifts in precipitation from land to ocean, as occurs during El Niño, can have a profound effect on tropical soils, as witnessed by the severe droughts over Indonesia and failure of the monsoon. We submit that the El Niño–stadial association provides a plausible explanation for the lower atmospheric CO_2, CH_4, and N_2O observed in ice core records.

We conclude that the strongest case can be made for an El Niño–stadial linkage during the last 70 kyrs. At times of cooling at high latitudes, the tropical Pacific was experiencing either less-frequent or less-persistent El Niños. The notion that El Niño would have been the dominant state during a glacial contrasts sharply with previous modeling and low-resolution observational studies that have predicted stronger trade winds and a larger tropical thermocline tilt under glacial conditions (*34*, *35*). The new perspective on millennial climate variability in the tropics presents an important challenge to the climate community to find the physical forcing that causes reduced atmospheric convection in the western tropical Pacific and reduced trade wind strength at times of high-latitude cooling. The answers will likely shed important light on how and why the Earth's climate undergoes abrupt climate changes and the likelihood that an abrupt change will occur in the future.

References and Notes

1. B. K. Lindsley, *Nature* **380**, 243 (1996).
2. Data from the NOAA-CIRES Climate Diagnostics Center, Boulder, CO, available online at www.cdc.noaa.gov/.
3. M. K. Gagan *et al.*, *Quat. Sci. Rev.* **19**, 45 (2000).
4. F. E. Urban, J. E. Cole, J. T. Overpeck, *Nature* **407**, 989 (2000).
5. D. P. Schrag, *Paleoceanography* **14**, 97 (1999).
6. A. W. Tudhope *et al.*, *Science* **291**, 1511 (2001).
7. S. R. Troelstra, D. Kroon, *Neth. J. Sea Res.* **24**, 459 (1989).
8. D. Caron, personal communication based on live collections in Bermuda.
9. T. Sowers *et al.*, *Paleoceanography* **8**, 737 (1993).
10. D. W. Lea, D. K. Pak, H. J. Spero, *Science* **289**, 1719 (2000).
11. M. Bender, T. Sowers, L. Labeyrie, *Global Biogeochem. Cycles* **8**, 363 (1994).
12. N. J. Shackleton, *Science* **289**, 1897 (2000).
13. R. G. Fairbanks *et al.*, *Coral Reefs* **16**, 593 (1997).
14. J. I. Martinez, P. D. Deckker, A. R. Chivas, *Mar. Micropaleontol.* **32**, 311 (1997).
15. S. G. H. Philander, *El Niño, La Niña, and the Southern Oscillation* (Academic Press, New York, 1990).
16. M. J. McPhaden, *Science* **283**, 950 (1999).
17. M. A. Cane, *Science* **282**, 5386 (2002).
18. M. A. Cane, A. C. Clement, in *Mechanisms of Global Climate Change at Millennial Time Scales*, P. U. Clark, R. S. Webb, L. D. Keigwin, Eds., vol. 112 of Geophysical Monograph Series (American Geophysical Union, Washington, DC, 1999), pp. 373–384.
19. A. C. Clement, M. A. Cane, in *Mechanisms of Global Climate Change at Millennial Time Scales*, P. U. Clark, R. S. Webb, L. D. Keigwin, Eds., vol. 112 of Geophysical Monograph Series (American Geophysical Union, Washington, DC, 1999).
20. M. Cane, *Science* **282**, 59 (1998).
21. M. A. Altabet, M. J. Higginson, D. W. Murray, *Nature* **415** (2002).
22. Y. J. Wang *et al.*, *Science* **294**, 2345 (2001).
23. E. Emmer, R. C. Thunell, *Paleoceanography* **15**, 377 (1999).
24. R. S. Ganeshram, T. F. Pederson, S. E. Calvert, R. Francois, *Nature* **215**, 156 (2002).
25. C. Pride *et al.*, *Paleoceanography* **14**, 397 (1999).
26. L. C. Peterson, G. H. Haug, K.A. Hughen, U. Röhl, *Science* **290**, 1950 (2000).
27. National Center for Environmental Prediction, NOAA Web site www.cpc.ncep.noaa.gov.
28. R. J. Behl, J. P. Kennett, *Nature* 379, 243 (1996).
29. F. B. Schwing, P. M. Green, T. Murphree, *EOS* **80**, 262 (1999).
30. L. D. Stott *et al.*, *Nature* **407**, 367 (2000).
31. T. Blunier *et al.*, *Nature* **394**, 739 (1998).
32. J. Flückiger *et al.*, *Science* **285**, 227 (1999).
33. B. Stauffer *et al. Nature* **392**, 59 (1998).
34. A. B. G. Bush, S. G. H. Philander, *Science* **279**, 1341 (1998).
35. D. Andreasen, D. H., A. C. Ravelo, A. J. Broccoli, *J. Geophys. Res.* **106,** 879 (2001).

36. We thank the NSF for supporting this research. We acknowledge the careful analytical assistance of M. Rincon.

Supporting Online Material
www.sciencemag.org/cgi/content/full/297/5579/222/DC1
Materials and Methods
Figs. S1 to S3
Table S1
References and Notes

7 March 2002; accepted 22 May 2002

REPORTS

El Niño–Like Pattern in Ice Age Tropical Pacific Sea Surface Temperature

Athanasios Koutavas,[1]* Jean Lynch-Stieglitz,[1] Thomas M. Marchitto Jr.,[1] Julian P. Sachs[2]

Sea surface temperatures (SSTs) in the cold tongue of the eastern equatorial Pacific exert powerful controls on global atmospheric circulation patterns. We examined climate variability in this region from the Last Glacial Maximum (LGM) to the present, using a SST record reconstructed from magnesium/calcium ratios in foraminifera from sea-floor sediments near the Galápagos Islands. Cold-tongue SST varied coherently with precession-induced changes in seasonality during the past 30,000 years. Observed LGM cooling of just 1.2°C implies a relaxation of tropical temperature gradients, weakened Hadley and Walker circulation, southward shift of the Intertropical Convergence Zone, and a persistent El Niño–like pattern in the tropical Pacific. This is contrasted with mid-Holocene cooling suggestive of a La Niña–like pattern with enhanced SST gradients and strengthened trade winds. Our results support a potent role for altered tropical Pacific SST gradients in global climate variations.

Studies of El Niño–Southern Oscillation (ENSO) dynamics and impacts demonstrate that the tropical Pacific ocean-atmosphere system influences global climate on interannual to decadal time scales (*1*). Models suggest that this system is sensitive to orbital forcing, dominated by precession in the tropics, which modulates the annual insolation cycle and affects the seasonal strength of winds and intensity of upwelling (*2*). Orbital perturbations of the seasonal cycle are believed to be critical determinants of the long-term behavior of ENSO (*2*). Proxy hydrographic records from the tropical Pacific document significant spectral power at precessional periods [19 to 23 thousand years (ky)] (*3*, *4*), but the specific mechanisms by which precession affects basin-scale ocean-atmosphere dynamics and their interaction with global climate remain elusive. Paleoclimatic evidence bearing on these questions is scant because of a lack of detailed, well-dated climate records from this region. In this study, we focus on the cold tongue of the eastern equatorial Pacific (EEP), where the

[1]Lamont-Doherty Earth Observatory and Department of Earth and Environmental Sciences, Columbia University, Palisades, NY 10964, USA. [2]Department of Earth, Atmospheric, and Planetary Sciences, Massachusetts Institute of Technology, 77 Massachusetts Avenue, Cambridge, MA 02139, USA.

*To whom correspondence should be addressed. E-mail: athan@ldeo.columbia.edu

largest ENSO signal occurs. We present a ^{14}C-dated Mg/Ca record of SST from near the Galápagos Islands and use it to evaluate changes in tropical Pacific SST patterns over the past 30 ky.

Cold-tongue SSTs are sensitive to changes in local wind patterns because of the presence of a shallow thermocline, which allows large SST anomalies to be induced by moderate changes in winds (*5*). This is evident in the large seasonal and interannual SST amplitudes in the cold tongue (5° to 10°C) compared with minimal changes in the western Pacific warm pool (1°C), where the thermocline is much deeper. The cold tongue itself is best developed south of the equator (*5*). Mean annual SST increases to the north, reaching a maximum at 10°N, the mean position of the Intertropical Convergence Zone (ITCZ) (Fig. 1). The cross-equatorial oceanographic gradient north of the Galápagos Islands is sharpest during seasonal upwelling events (August to September), when the cold tongue is fully developed, and relaxes in the warm season (February to March) and during El Niño, when the upwelling diminishes. To minimize the complicating influence of this gradient, we have selected for study a site south of the equator and near the core of the upwelling system.

Core V21-30 (1°13′S, 89°41′W, 617 m water depth) was raised just north of Española Island in the Galápagos Archipelago (Fig. 1). The shallow depth and unusually high sedimentation rates at this site (an average of 13 cm/ky over the past 30 ky) minimize postdepositional alteration problems associated with carbonate dissolution and bioturbation, and its position south of the equator makes it optimal for monitoring cold-tongue hydrographic properties. Sediment samples, each averaging ~50 to 100 years of deposition, were taken at 5-cm intervals or a mean temporal resolution of 450 years. We measured the oxygen isotope ratios (δ^{18}O) of the planktonic foraminifer *Globigerinoides sacculifer* (Fig. 2B), a species inhabiting the surface mixed layer, because of its association with photosynthetic symbionts (*6*). Although this species is believed to accrete up to 30% of its shell mass near the thermocline (*7*), observed core-top δ^{18}O values in V21-30 are consistent with annual mean temperature and salinity at the surface (*6*). This result indicates that the overall ecologic preference of *G. sacculifer* at this site renders it a useful recorder of surface hydrography, with only minor subsurface influence. In order to obtain explicit estimates of SST variations at this site, we applied Mg/Ca paleothermometry to this species. Uptake of Mg by planktonic foraminifera increases exponentially with ambient water temperature, as shown by core-top and culture calibration studies (*6*). Our results from V21-30 (table S1) are shown in Fig. 2C. The amplitude of reconstructed SST variations over the past 30 ky is about 2°C. Average SST during the Last Glacial Maximum (LGM) [23 to 19 ky before the present (B.P.)] is estimated from Mg/Ca to be 1.2° ± 0.3°C less than the average SST during the late Holocene (4.5 to 0 ky B.P.) (Fig. 2C). This estimate is supported by the δ^{18}O of *G. sacculifer* (Fig. 2B), which records a mean late Holocene–LGM change of 1.2 ± 0.15 per mil (‰). After correcting for an ice-volume effect of 1.0‰ (*8*), the implied mean LGM SST was 1° ± 0.7°C less than late Holocene values, assuming no change in seawater δ^{18}O associated with salinity effects. An independent estimate of LGM SST at this site from alkenone paleothermometry similarly indicates that temperatures were cooler by 1.2°C (*9*). The convergence of three independent proxies suggests that they are capturing the true amplitude of glacial-interglacial SST change at this site, averaging 1.2°C. This result is further supported by additional oxygen isotope data from neighboring cold-tongue sites (table S2). This finding is incongruous with recent reconstructions using radiolarian and foraminiferal transfer functions (*10*, *11*), which suggest that LGM cold-tongue temperatures were lower by 3° to 5°C. Because these methods are complicated by no-analog problems and, in the case of foraminifera, selective species removal by dissolution, we believe that a geochemical approach based on multiple proxies is better suited to this region.

Mg/Ca evidence from sites north of the Galápagos Islands (*3*) indicates that mean LGM SSTs were 2.5° to 3.0°C less than in the late Holocene, exceeding our estimate from V21-30 by at least a factor of 2. The emerging north-south pattern of LGM SST anomalies from these records indicates a reduction of the eastern Pacific cross-equatorial gradient. At present, a reduced gradient occurs seasonally in boreal winter and interannually during El Niño. It is accompanied by a southward shift of the ITCZ and contraction of the cold tongue as the northeast trades intensify and southeast trades weaken. We propose that, in analogous manner, the ITCZ was displaced southward during the LGM. Such a shift is consistent with evidence indicating

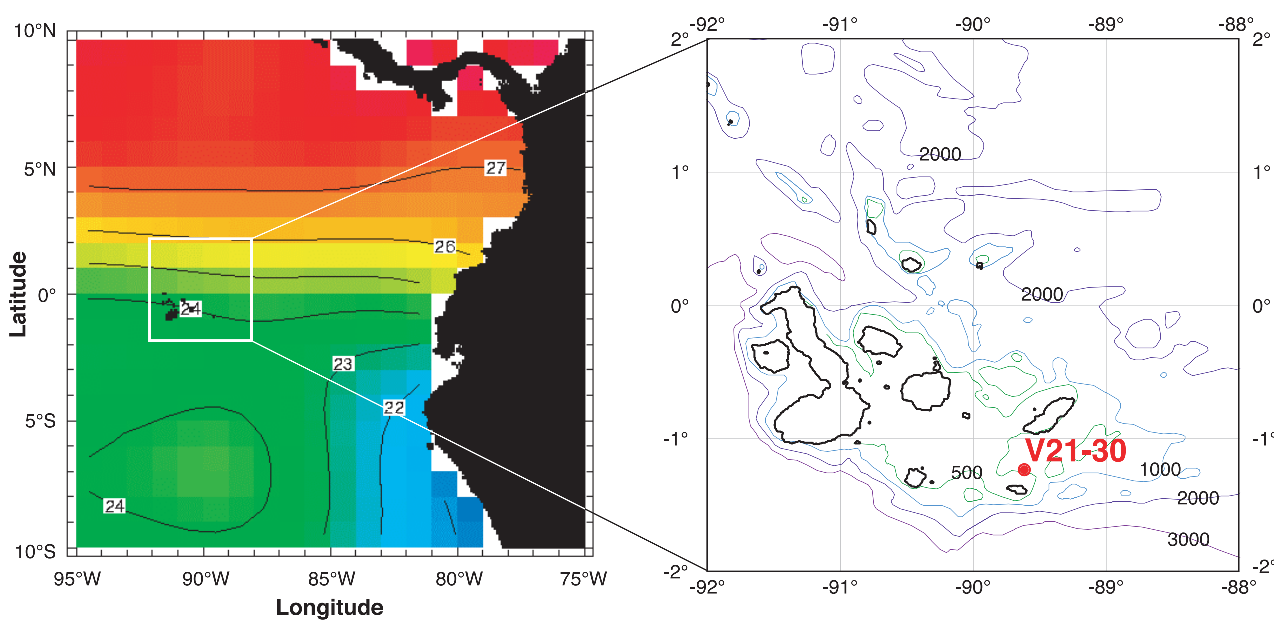

Fig. 1. Annual mean SST structure (°C) in the EEP (*35*) (**left**), and bathymetric contours (m) in the Galápagos Archipelago with location of site V21-30 (**right**).

wetter climate in the Bolivian Altiplano (*12*), drier climate in northern South America (*13*), and a southward shift of the Atlantic ITCZ (*14*, *15*). A reduction of the cross-equatorial (meridional) gradient in the EEP would tend to weaken the intensity of the Hadley cell (*16*). Weaker LGM Hadley circulation has been inferred from a pattern of drier tropics–wetter subtropics indicated by paleo–lake levels (*17*) and dust concentrations in Andean ice cores (*18*).

We test the alternative hypothesis that the LGM SST structure in the tropical Pacific resembled a La Niña–like pattern, with an enhanced east-west (zonal) gradient (*3*) and a steeper thermocline tilt. This hypothesis calls for intensified upwelling in the cold tongue due to stronger trade winds caused by the overall increase of the equator-to-pole temperature gradient. However, as the lower limb of the Hadley cell, trade wind circulation is more sensitive to the low-latitude gradient (*16*), which we find was reduced. Further, a southward shift of the ITCZ may have counteracted any increase in winds by shifting the zone of diminished wind strength closer to the equator, suppressing an upwelling response. We evaluated the zonal gradient in the equatorial Pacific by comparing our cooling estimate from V21-30 with estimates from the western Pacific. Records from the warm pool (*3*) and adjacent marginal basins such as the South China Sea (SCS) (*19*, *20*) indicate a range of LGM cooling from 2.5° to 4°C, which exceeds our estimate of 1° to 1.5°C for the cold tongue. This implies a reduced east-west gradient and therefore weaker Walker circulation and trade winds. Hence, we propose that the LGM temperature pattern in the tropical Pacific was more El Niño–like, with reduced zonal and meridional low-latitude gradients and a cooler background level. Possible mechanisms for this pattern include weaker atmospheric convection over the warm pool and ITCZ due to ocean cooling and reduced tropospheric greenhouse heating due to lower water vapor and CO_2 levels.

Lea *et al.* (*3*) showed that Pleistocene SST variations in the EEP consistently led changes in ice volume as reflected in $\delta^{18}O$. However, a precise chronology of the last deglaciation in the cold-tongue region has been lacking. Our ^{14}C-dated record confirms a lead of Mg/Ca SST over $\delta^{18}O$ by several millennia (Fig. 2, B and C) and indicates that post-LGM warming occurred between 20 and 17 ky B.P., during a maximum in equatorial seasonality (Fig. 2C). Experiments with a model of the tropical Pacific show that increased seasonality (reduced insolation in the upwelling season, August to September) favors the growth of El Niño events by weakening the trades and results in warmer mean cold-tongue temperatures (*2*). The modeled response of ENSO to orbital forcing predicts a sharp increase in warm (El Niño) events between 21 and 17 ky B.P. (*2*), matching the timing of warming in V21-30. The midpoint of observed warming at ~19 ky B.P. (Fig. 2C) coincides with the initial pulse of sea level rise after the LGM low stand, also dated to 19 ky B.P. (*21*). This indicates that cold-tongue dynamics were influential in halting global ice growth and initiating ice decay at the end of the LGM. Comparison with Antarctic climate as recorded in the Byrd ice core (Fig. 2E) shows synchronous cold-tongue warming and deglacial inception in Antarctica. This synchrony may result from dynamical coupling of the type observed presently during ENSO events (*22*) as an avenue for transmitting orbitally induced tropical SST anomalies to the Antarctic region. Further, advection of subantarctic water masses via the Equatorial Undercurrent (*23*) may have provided a positive climatic feedback between the two regions.

The period between 15 and 10 ky B.P. is marked by large high-frequency SST variations in V21-30 (Fig. 2C). The pattern of variability at this time suggests an inverse relation with Greenland temperature (Fig. 2A), most clearly seen at the onset of the rapid Bølling warming 14.8 ky B.P., when V21-30 reflects cooling by 1°C. Subsequent short-lived SST fluctuations persist until ~10 ky B.P. but cannot be definitively matched to the Greenland Ice Sheet Project Two (GISP2) ice-core record because of ^{14}C dating uncertainties. To further explore the nature of this variability and its effect on the equatorial Pacific zonal gradient, we compared our V21-30 SST record with the alkenone-based SST record from SCS core 18287-3 [obtained by Kienast *et al.* (*20*)] (Fig. 3). The SCS experienced abrupt warming in phase with Greenland at ~14.8 ky B.P., whereas temperature in the cold tongue dropped. This pattern implies an abrupt increase of the zonal gradient by ~2°C and a shift toward more La

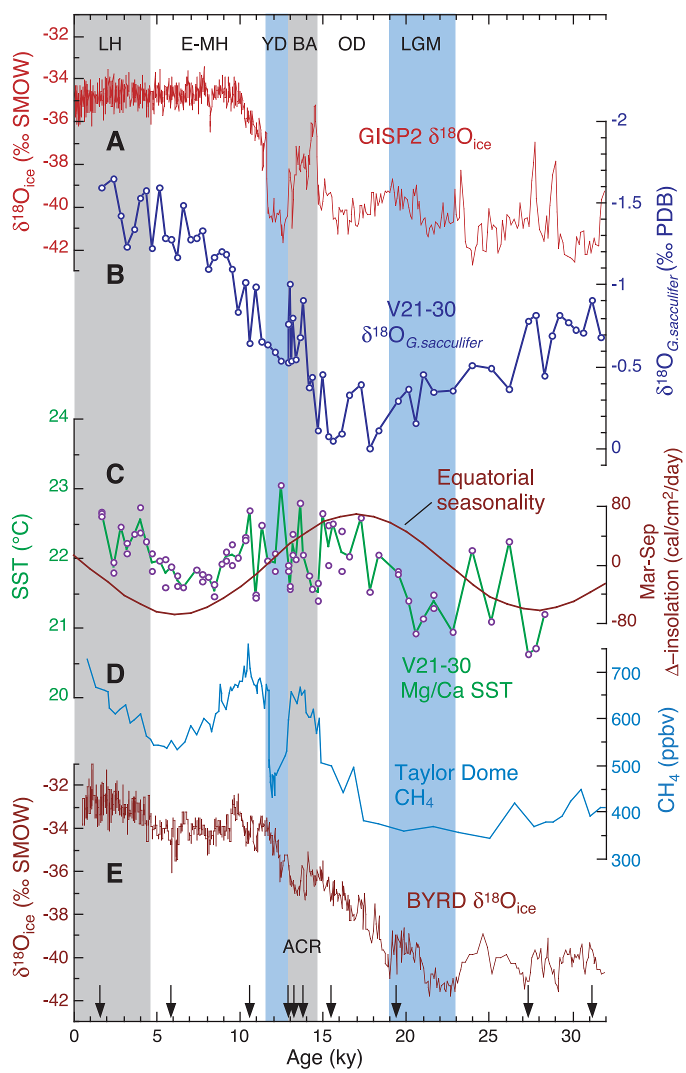

Fig. 2. Comparison of the climate evolution in EEP core V21-30 with temperature records from Greenland and Antarctica. (**A**) $\delta^{18}O_{ice}$ of the GISP2 Greenland ice core (*36*). (**B**) $\delta^{18}O$ record of *G. sacculifer* from V21-30. (**C**) Mg/Ca SST record of *G. sacculifer* from V21-30. The green line traces the mean of replicate analyses where available (mean Mg/Ca reproducibility of ±0.038 mmol/mol) and individual data points where no replicates were made. SST was calculated with the calibration data of Nürnberg *et al.* (*37*) as described in (*6*). The solid red line shows the insolation difference between March (warm season) and September (upwelling season) at the equator as a measure of seasonality in the cold tongue. (**D**) CH_4 concentrations in air trapped in the Taylor Dome ice core, Antarctica (*38*). (**E**) $\delta^{18}O_{ice}$ of the Byrd ice core, Antarctica (*39*). Climatic intervals are abbreviated as follows: LH, late Holocene; E-MH, early-to-middle Holocene; YD, Younger Dryas; BA, Bølling-Allerød; OD, Oldest Dryas; ACR, Antarctic Cold Reversal. Arrows at bottom indicate ^{14}C age-control points used in constructing the age model of V21-30 (table S3).

Niña–like conditions at the time of the Bølling warming. During the Younger Dryas the gradient decreased, primarily because of cooling in the SCS, then increased to near-present values by ~11 ky B.P. Overall, the observed pattern suggests a link between millennial-scale Greenland warming and establishment of a strong zonal gradient in the tropical Pacific and between cooling and a weak zonal gradient. Improvements in resolution, dating, and spatial coverage of tropical climate records are required to more accurately describe the millennial-scale climate pattern in the Pacific and its links with high latitudes.

Holocene variability in the cold tongue is of special interest because of mounting evidence for changing ENSO behavior during this time, in response to forcing by precession. A gradual decline in seasonality after 15 ky B.P. reached a broad minimum in the mid-Holocene (5 to 8 ky B.P.), which is mirrored by a broad SST minimum in V21-30 (Fig. 2C). Reduced or absent El Niño activity during this time is inferred from western Pacific corals (*24*), pollen evidence from Australia (*25*), and a lake record from Ecuador (*26*). A modeling study found reduced mid-Holocene SSTs in the EEP, because of strengthened zonal winds and enhanced upwelling, in response to precession (*27*). In accord with these studies, our data indicate that cooler and relatively stable SSTs prevailed in the cold tongue during this period. The zonal SST gradient in the equatorial Pacific was enhanced by ~0.5°C (Fig. 3), consistent with stronger trades and more vigorous Walker circulation. Some authors have inferred mid-Holocene warming in coastal northern Peru on the basis of geoarcheologic evidence (*28*, *29*), in discord with our finding of cooling. This disagreement may indicate that either (i) coastal Peru sites do not faithfully capture long-term SST trends in the cold tongue or (ii) their evidence requires a more complex interpretation.

Our record offers potential insights into the Holocene history of atmospheric methane concentrations. The mid-Holocene decrease in methane (Fig. 2D) has been attributed in part to weaker tropical wetland sources (*30*), despite evidence for intensified monsoon circulation (*31*) with wetter conditions and expanded vegetation cover in northern Africa, India, and Australia (*25*, *32*). This decrease seems to require that the bulk of the reduction in tropical methane sources occurred in South America, consistent with pollen evidence for the expansion of savanna at the expense of Amazonian rainforest in Bolivia (*33*). The methane decline over the first half of the Holocene is correlative with reduced SST in V21-30 (Fig. 2C). We suggest that persistent cold-tongue upwelling, inactive ENSO, and reduced seasonality in the mid-Holocene limited the ability of the ITCZ to penetrate southward during austral summer, depriving the southern margin of Amazonia of moisture. As cold-tongue temperatures rose in the late Holocene, ENSO became more active (*26*), Amazonian rainforests expanded (*33*), and atmospheric methane increased (Fig. 2D). Pre-Holocene methane variations do not appear directly related to V21-30 SST, which we attribute to the more complex pattern of global source variations during deglaciation.

Our data demonstrate that cold-tongue SST varied with the modulation of seasonality by precession during the past 30 ky, confirming the sensitivity of this system to insolation forcing (*2*). Despite their small amplitude, the timing of observed variations supports a central role for tropical Pacific dynamics in the global climate progression from the LGM to the late Holocene. Our finding of altered SST gradients in the past allows for large global impacts in accord with models (*34*) and supports the notion that sustained changes in tropical SSTs and their spatial patterns have profound long-term effects on global climate.

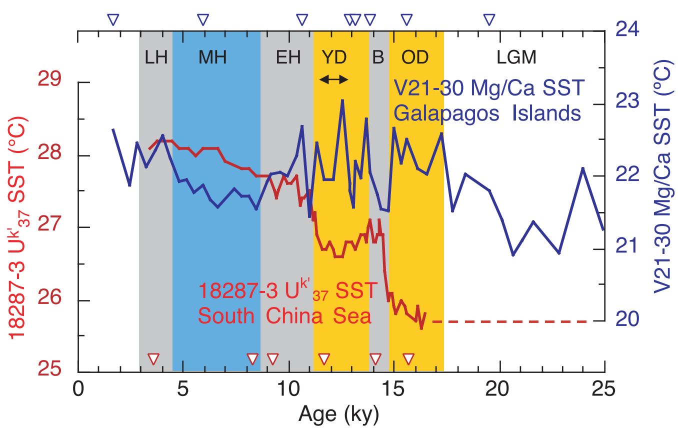

Fig. 3. Comparison of eastern and western equatorial Pacific SST history during the last deglaciation and Holocene. Mg/Ca SST data from V21-30 (blue line) are used as representative of the cold tongue, and alkenone ($U^{k'}_{37}$) SST data from SCS core 18287-3 (5°39′N, 110°39′E, 598 m depth) (red line) (*20*) as representative of the warm pool. Blue triangles (**top**) and red triangles (**bottom**) show ^{14}C age-control points for V21-30 (table S3) and 18287-3 (*20*), respectively. Climatic intervals are abbreviated as in Fig. 2. The dashed red line is a hypothetical extrapolation of the 18287-3 SST record to the LGM based on longer, lower resolution records from nearby sites (*19*). The two records are plotted to match in the LH. Past deviations in the east-west SST gradient relative to the LH are indicated by the offset between the two records (readable on either SST axis) and are highlighted with color bands as follows: blue, enhanced gradient; yellow, reduced gradient; gray, gradient similar to LH. The strongest gradient is observed during the mid-Holocene (MH, ~5 to 8 ky B.P., blue band) and coincides with minimum seasonality of insolation (Fig. 2C). The weakest gradient is observed during the OD (14.8 to 17 ky B.P.), when seasonality was at a maximum. In general, a reduced gradient is observed during cool periods in northern high latitudes (LGM, OD, and YD). A similar or enhanced gradient is observed during warm periods in northern high latitudes, including the Bølling (B) and the early and middle Holocene. The rapid warming of the Bølling interstadial at 14.8 ky B.P. is marked by a large, abrupt increase in the equatorial Pacific gradient by 2°C.

References and Notes

1. K. E. Trenberth *et al.*, *J. Geophys. Res.* **103**, 14291 (1998).
2. A. C. Clement, R. Seager, M. A. Cane, *Paleoceanography* **14**, 441 (1999).
3. D. W. Lea, D. K. Pak, H. J. Spero, *Science* **289**, 1719 (2000).
4. L. Beaufort, T. de Garidel-Thoron, A. C. Mix, N. G. Pisias, *Science* **293**, 2440 (2001).
5. A. V. Fedorov, S. G. Philander, *Science* **288**, 1997 (2000).
6. Materials and methods are available as supporting material on *Science* Online.
7. Y. Rosenthal, G. P. Lohmann, K. C. Lohmann, R. M. Sherrell, *Paleoceanography* **15**, 135 (2000).
8. D. P. Schrag, G. Hampt, D. W. Murray, *Science* **272**, 1930 (1996).
9. Alkenone unsaturation ratios ($U^{k'}_{37}$) were measured in three glacial samples (26.5 to 19.5 ky B.P.) and three Holocene samples (5.5 to 2.3 ky B.P.). Glacial age samples gave a mean SST of 23.84° ± 0.1°C, as compared to a mean Holocene SST of 25.0° ± 0.2°C.
10. N. G. Pisias, A. C. Mix, *Paleoceanography* **12**, 381 (1997).
11. C. Mix, A. E. Morey, N. G. Pisias, S. W. Hostetler, *Paleoceanography* **14**, 350 (1999).
12. P. A. Baker *et al.*, *Nature* **409**, 698 (2001).
13. C. M. Clapperton, *Palaeogeog. Palaeoclimatol. Palaeoecol.* **101**, 189 (1993).
14. L. C. Peterson, G. H. Haug, K. A. Hughen, U. Röhl, *Science* **290**, 1947 (2000).
15. A. Vink *et al.*, *Paleoceanography* **16**, 479 (2001).
16. D. Rind, *J. Geophys. Res.* **103**, 5943 (1998).
17. F. A. Street-Perrott, S. P. Harrison, in *Climate Processes and Climate Sensitivity*, vol. 29 of *Geophysical Monograph Series*, J. E. Hansen and T. Takahashi, Eds. (American Geophysical Union, Washington, DC, 1984), pp. 118–129.
18. L. G. Thompson *et al.*, *Science* **282**, 1858 (1998).
19. C. Pelejero, J. O. Grimalt, S. Heilig, M. Kienast, L. Wang, *Paleoceanography* **14**, 224 (1999).
20. M. Kienast, S. Steinke, K. Stattegger, S. E. Calvert, *Science* **291**, 2132 (2001).
21. Y. Yokoyama, K. Lambeck, P. De Deckker, P. Johnston, L. K. Fifield, *Nature* **406**, 713 (2000).
22. W. B. White, R. G. Peterson, *Nature* **380**, 699 (1996).
23. J. R. Toggweiler, K. Dixon, W. S. Broecker, *J. Geophys. Res.* **96**, 20467 (1991).
24. A. W. Tudhope *et al.*, *Science* **291**, 1511 (2001).
25. J. Shulmeister, B. G. Lees, *The Holocene* **5**, 10 (1995).
26. D. T. Rodbell *et al.*, *Science* **283**, 516 (1999).
27. A. C. Clement, R. Seager, M. A. Cane, *Paleoceanography* **15**, 731 (2000).
28. D. H. Sandweiss, J. B. Richardson III, E. J. Reitz, H. B. Rollins, K. A. Maasch, *Science* **273**, 1531 (1996).
29. C. F. T. Andrus, D. E. Crowe, D. E. Sandweiss, E. J. Reitz, C. S. Romanek, *Science* **295**, 1508 (2002).

30. J. Chappellaz *et al.*, *J. Geophys. Res.* **102**, 15987 (1997).
31. S. Joussaume *et al.*, *Geophys. Res. Lett.* **26**, 859 (1999).
32. COHMAP Members, *Science* **241**, 1043 (1988).
33. F. E. Mayle, R. Burbridge, T. J. Killeen, *Science* **290**, 2291 (2000).
34. J. H. Yin, D. S. Battisti, *J. Clim.* **14**, 565 (2001).
35. S. Levitus, T. P. Boyer, *World Ocean Atlas 1994, Volume 4: Temperature*, NOAA Atlas NESDIS (U.S. Department of Commerce, Washington, DC, 1994).
36. P. M. Grootes, M. Stuiver, *J. Geophys. Res.* **102**, 26455 (1997).
37. D. Nürnberg, J. Bijma, C. Hemleben, *Geochim. Cosmochim. Acta* **60**, 803 (1996).
38. E. J. Brook, S. Harder, J. Severinghaus, E. J. Steig, C. M. Sucher, *Global Biogeochem. Cycles* **14**, 559 (2000).
39. T. Blunier, E. J. Brook, *Science* **291**, 109 (2001).
40. We thank P. deMenocal and A. van Geen for lab equipment and facilities; M. A. Cane, J. C. H. Chiang, and U. S. Ninnemann for helpful comments; M. Kienast for data; and J. Hayes at the National Ocean Sciences Accelerator Mass Spectrometry Facility for support with ^{14}C analyses. Supported by grants from NSF and a grants/cooperative agreement from the National Oceanic and Atmospheric Administration (NOAA). The views expressed herein are those of the authors and do not necessarily reflect the views of NOAA or any of its subagencies. Support for the curating facilities of the Lamont-Doherty Earth Observatory (LDEO) Deep-Sea Sample Repository is provided by NSF and the Office of Naval Research. Portions of this work were also supported by the LDEO Climate Center.

Supporting Online Material
www.sciencemag.org/cgi/content/full/297/5579/226/DC1
Materials and Methods
Tables S1 to S3

29 March 2002; accepted 30 May 2002

Two-Dimensional X-ray Waveguides and Point Sources

F. Pfeiffer,[1] C. David,[2] M. Burghammer,[3] C. Riekel,[3] T. Salditt[1]*

We show that resonant coupling of synchrotron beams into suitable nanostructures can be used for the generation of coherent x-ray point sources. A two-dimensionally confining x-ray waveguide structure has been fabricated by e-beam lithography. By shining a parallel undulator beam onto the structure, a discrete set of resonant modes can be excited in the dielectric cavity, depending on the two orthogonal coupling angles between the beam and the waveguide interfaces. The resonant excitation of the modes is evidenced from the characteristic set of coupling angles as well as the observed far-field pattern. The x-ray nanostructure may be used as coherent x-ray point sources with a beam cross section in the nanometer range.

X-ray scattering has had a tremendous impact as an experimental technique for studying the atomic structure of condensed matter. However, the technique is usually limited by two important constraints. First, it is characterized by two extremely opposed (separated) length scales: the microscopic x-ray wavelength $\lambda \cong 0.1$ nm and the macroscopic cross section D of the beam or, equivalently, the spot size on the sample. The sample therefore must be homogeneous over the entire length D, and the technique probes its ensemble-averaged structure. Second, the technique is restricted to static structural information owing to the elastic nature of the scattering events. X-ray scattering is insensitive to the dynamic nature of structural assemblies.

While synchrotron-based inelastic x-ray scattering and photon correlation spectroscopy address the second constraint, microbeam techniques challenge the first (*1*, *2*). If both constraints are to be circumvented simultaneously, small, intense, and fully coherent x-ray beams are needed. Micrometer-sized pinholes are currently used in photon correlation spectroscopy (*3*), but smaller coherent beams of $D \cong 10$ to 100 nm cannot be achieved by pinholes. Even if hypothetical pinholes of such size were available, the flux throughput would be insufficient. Spot sizes of ~90 nm have been obtained in the range of 5 to 8 keV by glass capillary optics (*1*), but these optics do not preserve coherence. Focused spot sizes of coherent beams can be achieved in the range of tens of nanometers for soft x-rays (*4*) by using diffractive lenses (Fresnel zone plates). However, because of the strong decrease of the absorption and phase shift with increasing photon energy, it becomes increasingly difficult to obtain small spot sizes at photon energies of 8 keV and above, and to our knowledge, no coherently focused spot sizes of less than several 100 nm have been reported to date (*5*).

X-ray waveguide structures present an approach for producing a coherent and divergent x-ray beam with precisely defined properties concerning shape and coherence (*6*), based on the principle of resonant beam coupling. The size of the beam at the exit of the waveguide is smaller than the thickness d of the waveguiding layer, which may reach down to $d \cong 10$ nm (*7*). The flux is efficiently increased by internal resonant field enhancement due to the generation of modes. Lensless projection phase contrast microscopy (*8*), as well as x-ray diffraction with submicrometer spatial resolution, has been demonstrated (*9*). The samples can be positioned outside the x-ray waveguide in the exiting beam or can be directly incorporated in the device. Macromolecular films (*10*) and colloidal suspensions (*11*) have already been investigated inside the resonantly enhanced field of a waveguide structure, making up its guiding layer.

To date, x-ray waveguide optics have been exclusively one-dimensional (1D), whereas most nanobeam applications would require two-dimensional (2D) point beams instead of 1D line beams. We present a proof of principle that the concept of resonant beam coupling can be generalized to two dimensions. To this end, we fabricated a rectangular x-ray waveguide by e-beam lithography, which compresses hard x-ray beams in two dimensions.

Visible light and infrared waveguides used in integrated optics are made of a rectangular dielectric core material, typically with an index of refraction in the range between 1.3 and 1.6, embedded in a dielectric cladding of a lower index to allow for guided mode propagation. The principal geometry of a rectangular waveguide is shown in Fig. 1, with width w and height h in the micrometer range. Contrarily, the index of refraction for hard x-rays $n = 1 - \delta + i\beta$ is always slightly smaller than 1, in proportion to the electron density of the material (*12*). The core material must therefore have a low electron density and yet also have a low absorption coefficient, and the cladding material with a comparably high electron density must provide a sufficiently high potential wall for the formation of guided modes. Apart from the optical constants, an important constraint is given by the condition that the chosen materials must be compatible with currently available lithography techniques to reach w and h values in the range of 100 nm and below. Considering these requirements, a combination of poly(methyl methacrylate) (PMMA) as a core material with a Cr cladding was chosen.

In order to analytically analyze the guiding characteristics of an x-ray waveguide and to optimize the design parameters, one has to solve the scalar wave equation

$$\nabla^2\Psi(x, z) + n^2(x, z)k^2\Psi(x, z) = 0 \quad (1)$$

for the electromagnetic field $\Psi(x, z)$, where $\nabla^2 = \partial^2/\partial x^2 + \partial^2/\partial z^2$, $k = 2\pi/\lambda$, and $n(x, z)$ is the profile of the refractive index given by the geometry of the guide (*13*). An exact

[1]Universität des Saarlandes, Im Stadtwald 38, Postfach 15 11 50, 66041 Saarbrücken, Germany. [2]Laboratory for Micro- and Nanotechnology, Paul Scherrer Institut, CH-5232 Villingen-PSI, Switzerland. [3]European Synchrotron Radiation Facility, Boite Postale 220, F-38043 Grenoble Cedex, France.

*To whom correspondence should be addressed. E-mail: salditt@mx.uni-saarland.de